AIMS Mathematics, 11(9): 29816–29847.
DOI: 10.3934/math.20261183
Received: 29 July 2026
Revised: 31 August 2026
Accepted: 07 September 2026
Published: 15 September 2026

https://www.aimspress.com/journal/Math

Research article

A ψ-fractal-fractional Atangana–Baleanu model for a nonlinear memristive integrator circuit: analysis and numerical approximation

Osman Abdalla Osman*, Muntasir Suhail, Mohammed Rabih and Habeeb Ibrahim

Department of Mathematics, College of Science, Qassim University, Buraydah 51452, Saudi Arabia; m.suhail@qu.edu.sa, M.Fadlallah@qu.edu.sa, ha.ibrahim@qu.edu.sa

* **Correspondence:** Email: o.osman@qu.edu.sa.

Abstract: This work develops an Atangana–Baleanu (AB)–ψ-fractal-fractional (ABFF) model for a nonlinear memristive integrator circuit using an outer-derivative construction. The Atangana–Baleanu derivative in Caputo (ABC) sense and the Atangana–Baleanu derivative in Riemann (ABR) sense are distinguished explicitly throughout. The raw outer derivative is a ψ-weighted ABR operator; therefore, a classical initial-value problem is posed for the regularized state $v - v(0)$, which is exactly equivalent to a weighted ABC equation. The resulting Volterra formulation contains the operational-clock density $\omega_{\psi,\theta}(t) = \theta[\psi(t) - \psi(0)]^{\theta-1}\psi'(t)$ in both the instantaneous and hereditary terms. We establish explicit growth and local Lipschitz estimates, a Krasnosel'skii existence result, a continuation criterion, and finite-time uniqueness and continuous-dependence estimates based on a fractional Gronwall argument. Importantly, the revised uniqueness and Ulam–Hyers estimates require contraction only of the instantaneous AB term and no longer impose a smallness condition that grows like T^{γ}. Generalized Ulam–Hyers–Rassias stability is reformulated in a weighted norm. A two-step product-integration method is derived, and a full first-order convergence theorem is proved under a bounded endpoint density. An exact scalar Volterra benchmark confirms the predicted order. For the oscillatory circuit, terminal values and the uninformative initial-state maximum norm are replaced by post-transient amplitudes and periods. A necessary initial-compatibility condition at $t = 0$ is identified explicitly. All reported fractional circuit simulations use endpoint-compatible bounded clocks with $\omega_{\psi,\theta}(0)F(U_0) = 0$; in particular, the base clock $\psi_b(t) = t^2/(1 + t)$ is used for the fractional-order and fractal-exponent studies. This removes an otherwise hidden incompatibility between the nonsingular ABC kernel and the prescribed non-equilibrium initial state.

Keywords: fractional derivatives; ψ-fractal derivative; Atangana–Baleanu derivative; Mittag–Leffler kernel; memristive integrator circuit; Ulam–Hyers stability
Mathematics Subject Classification: 26A33, 34A08, 34A34, 65L05, 65L20

1. Introduction

Fractional differential equations have now become an established method for modeling dynamic phenomena in which the current state is influenced not only by instantaneous data but also by a distribution of past events. The classical works of Podlubny [1], Kilbas et al. [2], Diethelm [3], and Mainardi [4] provide a broad foundation for fractional initial-value problems, Mittag–Leffler functions, hereditary constitutive laws, and numerical methods. Together, these studies show that fractional modeling depends not only on the derivative order and kernel but also on how memory enters the dynamics. Petráš [5] provided a complementary treatment focused on nonlinear fractional-order systems.

An important development in fractional calculus was the introduction of fractional operators with nonsingular kernels. Caputo and Fabrizio [6] proposed an exponential-kernel derivative, and Losada and Nieto [7] subsequently studied its associated integral operator and basic differential equations. This work initiated a substantial line of regular-kernel modeling. Singh et al. [8], for example, applied the Caputo–Fabrizio derivative to a fractional model for computer-virus propagation. A more recent direction combined Mittag–Leffler and Caputo–Fabrizio features. Alqhtani et al. [9] introduced the Mittag-Leffler–Caputo–Fabrizio operator together with a numerical approach, while Sadek and Aldawish [10] studied the corresponding integral, established existence and uniqueness conditions, and developed a first-order numerical scheme.

This type of regular kernel direction has been taken further by Atangana and Baleanu [11] with the introduction of Caputo- and Riemann derivatives with a Mittag–Leffler kernel. What makes the Atangana–Baleanu (AB) approach particularly interesting for our purposes is that the integral involved in this approach contains an instantaneous and a hereditary part. Existence and uniqueness questions for ODEs of this kind have been explored by Jarad et al. [12]. Following this, Atangana [13] defined fractal-fractional calculus, with both a fractional memory term and a fractal scaling term. This additional degree of freedom is the immediate theoretical precursor of the generalized model developed here.

The fractal-fractional operators have already been employed for modeling nonlinear circuits. Akgül et al. [14] formulated a fractal-fractional AB nonlinear integrator circuit and analyzed the existence and uniqueness, Ulam–Hyers stability, numerical solutions, and phase portraits of the proposed system. Their model is the closest applied antecedent to the system studied in this paper. However, its fractal scale is tied to a fixed power-law clock. Here, that clock is replaced by a differentiable increasing function ψ, which separates three modeling ingredients: the Mittag–Leffler memory kernel, the fractal exponent, and the profile of operational time. Fractional-order integrator realizations have also been studied from an engineering perspective. Zourmba et al. [15] constructed a fractional integrator circuit using the Charef approximation, Krishna [16] surveyed realizations of fractional-order differentiators and integrators, and Podlubny et al. [17] presented analogue realizations of fractional-order controllers.

The nonlinear circuit considered here is also closely related to memristive systems. Chua [18] introduced the memristor as a fundamental circuit element relating charge and flux, and Strukov et al. [19] later reported a nanoscale device exhibiting memristive behavior. Chua [20] clarified the relation between resistance-switching memories and memristive signatures, while Yang et al. [21] reviewed applications of memristive devices in memory, logic, and neuromorphic computing.

The generalized local clock that is employed in this study uses the ψ-fractal derivative that was

proposed by Sadek et al. [22]. The fundamental concept is the measurement of the rate of change of the function locally with respect to a non-uniform operational scale instead of just physical time. Using the current notation, this clock is

$$\Xi_{\psi,\theta}(t) = [\psi(t) - \psi(0)]^{\theta} \tag{1}$$

with density

$$\omega_{\psi,\theta}(t) = \Xi'_{\psi,\theta}(t) = \theta[\psi(t) - \psi(0)]^{\theta-1}\psi'(t). \tag{2}$$

Thus, θ controls the fractal exponent, whereas ψ determines how the operational time is stretched or compressed along the physical time axis.

This concept corresponds to the more general idea of fractional derivatives with respect to another function. Specifically, in [23], a Caputo-like fractional derivative with respect to a function ψ was defined, and its basic properties and solutions were established; on the other hand, in [24], the ψ-Hilfer derivative was introduced, and an example of an auxiliary function was provided, helping to define a whole class of fractional derivatives. All this means that a non-uniform clock may offer modeling flexibility regardless of the fractional order. However, the fractional operator introduced in this manuscript is structurally distinct in the sense that while ψ appears in the outer fractal derivative (2), the time-lag variable $t - s$ still appears in the AB kernel.

In the present circuit analysis, ψ is therefore treated as a phenomenological operational-time map rather than as an additional resistance, capacitance, or memristor parameter. Polynomial, logarithmic, rational, and exponential choices of ψ are used only as sensitivity profiles for a nonuniform clock. A physical realization would require calibration of a fractional-order integrator whose input–output behavior reproduces the selected density $\omega_{\psi,\theta}$; that identification problem lies outside the scope of the present mathematical and computational study.

The applications of AB derivatives in non-linear and chaotic systems give additional insight into the current model. Alkahtani [25] investigated Chua's circuit using AB derivative, and Atangana and Koca [26] analyzed a chaotic system with AB derivatives. Both these models help to understand that the replacement of the classical derivative by a nonsingular memory effect can change the dynamics of the system. The current research incorporates the time-independent kernel ψ.

Numerical reliability is equally important because fractional discretizations accumulate the entire solution history. Consequently, a scheme should be assessed through consistency, stability, and convergence, rather than through trajectory plots alone. A solid numerical framework for fractional initial value problems was provided in the monograph of Diethelm [3], whereas Garrappa [27] reviewed various numerical schemes and their implementation. Regarding nonsingular kernels, Djida et al. [28] looked into the numerical evaluation of a derivative involving a nonlocal and nonsingular kernel; Toufik and Atangana [29] suggested a numerical scheme for evaluating these derivatives and applying it to chaotic systems; and Akgül [30] constructed a numerical scheme for fractional equations involving nonlocal and nonsingular kernels. All these references inspire us to devise an explicit history-based product integration scheme and, more importantly, the actual convergence analysis of the generalized circuit equation.

The literature, therefore, leaves a specific gap. Existing fractal-fractional AB circuit models use a fixed power-type operational scale, whereas the literature on ψ-dependent operators allows the operational time to vary but does not address the present weighted AB circuit structure. In particular, we are not aware of a convergence analysis for an AB circuit discretization in which the nonlinear

vector field is multiplied by the generalized density $\omega_{\psi,\theta}$. The present paper connects these directions by developing an Atangana–Baleanu–ψ-fractal-fractional (ABFF) framework together with a first-order convergence theory for its explicit product-integration discretization.

Motivated by this gap, the fixed power-type fractal scale t^θ is replaced by the operational clock (1). Each of the variables γ, θ, and ψ has its own mathematical significance: γ manages the Mittag–Leffler memory, θ manages the fractal scaling, and ψ manages the unevenness of operational time. The key contributions can be summarized as follows:

(1) The outer derivative operation is called the ABFF derivative, and its notation is distinguished from the classical ABC and ABR derivatives. The nature of its ABR property, initial value regularization, inverse integral, reductions, and end-point behavior is explicitly stated.
(2) The nonlinear integrator circuit is expressed for $U - U_0$ and converted to a weighted ABC/Volterra equation. Evaluating that equation at the initial endpoint reveals the necessary compatibility condition $\omega_{\psi,\theta}(0)F(U_0) = 0$ for $0 < \gamma < 1$. Because the prescribed circuit state is not an equilibrium, the reported fractional simulations are built from clocks with zero endpoint density. The function ψ is interpreted within clear physical limits as an operational-time relationship that would require calibration against a controlled integrator circuit.
(3) Existence follows from a Krasnoselskii splitting and a continuation principle. Uniqueness, continuous dependence, and Ulam–Hyers stability are enhanced using fractional Gronwall inequalities that rely solely on contraction of the instantaneous AB term without the previous requirement $q < 1$. Ulam–Hyers–Rassias stability is given in the suitable weighted norm.
(4) Product integration comes with a stability lemma and a first-order convergence theorem. The exact scalar experiment confirms the predicted order, while circuit outcomes are described through post-transient amplitudes and periods rather than endpoint values. All fractional circuit experiments satisfy the bounded-density and initial-compatibility requirements; the convergence theorem additionally assumes the stated source smoothness.

The paper is organized as follows: Section 2 introduces the generalized operator and its limiting cases. Section 3 formulates the circuit and derives the weighted Volterra representation. Sections 4–6 contain the structural estimates, well-posedness results, and Ulam-type stability analysis. Section 7 gives the numerical derivation and implementation. Section 8 reports the simulations, an exact convergence benchmark, and an application-level refinement check based on oscillation statistics; the final section summarizes the conclusions.

2. Preliminaries and the ψ-fractal-fractional AB operator

2.1. Mittag–Leffler function and AB normalization

For $0 < \gamma \leq 1$, the one-parameter Mittag–Leffler function is

$$E_\gamma(z) = \sum_{k=0}^{\infty} \frac{z^k}{\Gamma(\gamma k + 1)}. \tag{3}$$

Let $B(\gamma)$ be a positive normalization satisfying $B(0) = B(1) = 1$. In all computations, we use

$$B(\gamma) = 1 - \gamma + \frac{\gamma}{\Gamma(\gamma)}. \tag{4}$$

For $0 < \gamma < 1$, the classical Atangana–Baleanu derivative in Caputo (ABC) sense [11] is

$$ {}^{ABC}_{0}D^{\gamma}_{t}v(t) = \frac{B(\gamma)}{1-\gamma}\int_0^t v'(s)E_{\gamma}\left(-\frac{\gamma}{1-\gamma}(t-s)^{\gamma}\right)ds, \qquad 0 < \gamma < 1. \tag{5} $$

For $0 < \gamma < 1$, the corresponding Atangana–Baleanu derivative in Riemann (ABR) sense is

$$ {}^{ABR}_{0}D^{\gamma}_{t}v(t) = \frac{B(\gamma)}{1-\gamma}\frac{d}{dt}\int_0^t v(s)E_{\gamma}\left(-\frac{\gamma}{1-\gamma}(t-s)^{\gamma}\right)ds, \qquad 0 < \gamma < 1. \tag{6} $$

The formulas containing $(1-\gamma)^{-1}$ are definitions for $0 < \gamma < 1$. The endpoint $\gamma = 1$ is used only through the standard limit $\gamma \to 1^{-}$, which gives the ordinary first derivative in the regularized formulation; it is not obtained by direct substitution into those singular prefactors.

For sufficiently regular v, the standard identity

$$ {}^{ABR}_{0}D^{\gamma}_{t}(v - v(0)) = {}^{ABC}_{0}D^{\gamma}_{t}v \tag{7} $$

holds. This identity is essential below: it permits classical initial data even though the new definition differentiates the convolution after it is formed.

Its associated fractional integral is

$$ {}^{AB}_{0}I^{\gamma}_{t}g(t) = \frac{1-\gamma}{B(\gamma)}g(t) + \frac{\gamma}{B(\gamma)\Gamma(\gamma)}\int_0^t (t-s)^{\gamma-1}g(s)\,ds. \tag{8} $$

2.2. The ψ-fractal derivative

Let ψ: $[0,T] \to \mathbb{R}$ be strictly increasing, continuous on $[0,T]$, continuously differentiable on $(0,T]$, and satisfy $\psi'(t) > 0$ for $t > 0$.

Definition 1. *[22] For $0 < \theta \leq 1$, the ψ-fractal derivative of a function v is*

$$ \frac{d^{\theta,\psi}v(t)}{dt^{\theta,0}} = \lim_{s\to t}\frac{v(s)-v(t)}{[\psi(s)-\psi(0)]^{\theta} - [\psi(t)-\psi(0)]^{\theta}}, \tag{9} $$

whenever the limit exists.

If v is differentiable and the denominator density does not vanish, then

$$ \frac{d^{\theta,\psi}v(t)}{dt^{\theta,0}} = \frac{v'(t)}{\omega_{\psi,\theta}(t)}, \qquad \omega_{\psi,\theta}(t) = \theta[\psi(t)-\psi(0)]^{\theta-1}\psi'(t). \tag{10} $$

Thus, this derivative is differentiable with respect to the generalized clock $\Xi_{\psi,\theta}$.

2.3. ABFF derivative

Definition 2. *(ABFF derivative) For $0 < \gamma < 1$ and $0 < \theta \leq 1$, define*

$$ {}^{ABFF}_{0}\mathbb{D}^{\gamma,\theta,\psi}_{t}v(t) = \frac{B(\gamma)}{1-\gamma}\frac{d^{\theta,\psi}}{dt^{\theta,0}}\int_0^t v(s)E_{\gamma}\left(-\frac{\gamma}{1-\gamma}(t-s)^{\gamma}\right)ds. \tag{11} $$

The abbreviation ABFF is used only for the new ABFF operator; ABC and ABR retain their standard meanings.

When the ψ-fractal derivative is represented by (10), Definition 2 becomes

$$ {}_0^{ABFF}\mathbb{D}_t^{\gamma,\theta,\psi} v(t) = \frac{1}{\omega_{\psi,\theta}(t)} {}_0^{ABR}D_t^{\gamma} v(t). \tag{12} $$

Hence, the raw outer-derivative expression is a ψ-weighted ABR operator and does not annihilate constants. A classical initial condition $v(0) = v_0$ is therefore imposed by applying the operator to $v - v_0$. At $\gamma = 1$, we understand the regularized operator by the limit $\gamma \to 1^-$.

Proposition 1. *(Initial-value regularization) Let v be absolutely continuous and let $\omega_{\psi,\theta}(t) > 0$ for $t > 0$. Then,*

$$ {}_0^{ABFF}\mathbb{D}_t^{\gamma,\theta,\psi}(v - v(0))(t) = \frac{1}{\omega_{\psi,\theta}(t)} {}_0^{ABC}D_t^{\gamma} v(t). \tag{13} $$

Proof. By (12) and the standard regularization identity (7),

$$ {}_0^{ABFF}\mathbb{D}_t^{\gamma,\theta,\psi}(v - v(0)) = \frac{1}{\omega_{\psi,\theta}(t)} {}_0^{ABR}D_t^{\gamma}(v - v(0)) = \frac{1}{\omega_{\psi,\theta}(t)} {}_0^{ABC}D_t^{\gamma} v. $$

This completes the proof. □

Definition 3. *(ABFF integral) For a continuous function g, define*

$$ {}_0^{ABFF}\mathbb{I}_t^{\gamma,\theta,\psi}\, g(t) = \frac{1-\gamma}{B(\gamma)}\omega_{\psi,\theta}(t)g(t) + \frac{\gamma}{B(\gamma)\Gamma(\gamma)}\int_0^t (t-s)^{\gamma-1}\omega_{\psi,\theta}(s)g(s)\,ds. \tag{14} $$

Proposition 2. *Let v be sufficiently regular. Then the raw operator satisfies*

$$ {}_0^{ABFF}\mathbb{I}_t^{\gamma,\theta,\psi}\left({}_0^{ABFF}\mathbb{D}_t^{\gamma,\theta,\psi}\, v\right)(t) = v(t), \tag{15} $$

whereas the regularized initial-value form satisfies

$$ {}_0^{ABFF}\mathbb{I}_t^{\gamma,\theta,\psi}\left({}_0^{ABFF}\mathbb{D}_t^{\gamma,\theta,\psi}(v - v(0))\right)(t) = v(t) - v(0). \tag{16} $$

Proof. Set

$$ g = {}_0^{ABFF}\mathbb{D}_t^{\gamma,\theta,\psi}\, v. $$

By (12),

$$ \omega_{\psi,\theta} g = {}_0^{ABR}D_t^{\gamma} v. $$

Substitution into Definition 3 gives the standard composition

$$ {}_0^{AB}I_t^{\gamma}({}_0^{ABR}D_t^{\gamma} v) = v, $$

which proves (15). Applying the same argument to $v - v(0)$ proves (16). Equivalently, Proposition 1 reduces the second statement to the standard ABC inverse identity. □

2.4. Special cases and endpoint behavior

Proposition 3. *The following reductions hold:*

(1) If $\psi(t) = t$ and $\theta = 1$, the raw operator becomes the standard ABR derivative, while its regularized form applied to $v - v(0)$ becomes the standard ABC derivative.

(2) If $\psi(t) = t$, then $\omega_{\psi,\theta}(t) = \theta t^{\theta-1}$ and the regularized model recovers the usual power-scale fractal–fractional AB initial-value equation.

(3) If $\theta = 1$, then $\omega_{\psi,\theta}(t) = \psi'(t)$, so the AB memory is modulated by the nonuniform operational clock ψ.

(4) Formally, as $\gamma \to 1^-$, the raw operator tends to the ψ-fractal derivative $v'(t)/\omega_{\psi,\theta}(t)$; the regularized and raw limits coincide because the derivative of a constant vanishes in the integer-order limit.

(5) If $\gamma = \theta = 1$ and $\psi(t) = t$, the regularized model reduces to the ordinary first-order initial-value problem.

For the uniform-norm theory and for every numerical experiment reported below, we impose the following endpoint-compatible hypothesis.

Assumption 1. *(Bounded density) The density $\omega_{\psi,\theta}$ has a bounded, nonnegative, continuous extension to $[0, T]$. We denote*

$$M_\omega = \max_{0\le t\le T} \omega_{\psi,\theta}(t).$$

The choice $\psi(t) = t$ with $0 < \theta < 1$ produces

$$\omega_{\psi,\theta}(t) = \theta t^{\theta-1},$$

which is unbounded at the origin and therefore lies outside Assumption 1. In the revised simulations, we do not regularize that singular clock. Instead, the fractal-order experiment uses

$$\psi_b(t) = \frac{t^2}{1+t}, \qquad \psi_b'(t) = \frac{t(2+t)}{(1+t)^2}. \tag{17}$$

For every $\theta > 1/2$, its density behaves as

$$\omega_{\psi,\theta}(t) \sim 2\theta t^{2\theta-1}$$

as $t \downarrow 0$ and therefore extends continuously and boundedly to the endpoint (with value 0 for every $\theta > 1/2$). This places the revised values $\theta \in \{1, 0.99, 0.98, 0.965\}$ inside the analytical setting.

Remark 1. *(Scope of the analytical results) Theorems 1–4 are proved under Assumption 1. Singular clocks such as $\psi(t) = t$, $0 < \theta < 1$, require a different weighted-space analysis and are not used as evidence for the present theorems. The long-time computations are numerical trajectories; the analytical continuation statement below explains precisely what additional boundedness is needed to extend a local solution to a prescribed finite horizon.*

3. The generalized integrator circuit model

3.1. Dimensionless nonlinear system

Throughout Sections 3–8, the symbol ${}_0^{ABFF}\mathbb{D}_t^{\gamma,\theta,\psi}$ denotes exactly the ABFF operator of Definition 2; ABC and ABR retain their standard meanings. With this notation, the circuit studied in [14] is generalized as follows:

$$\begin{cases} {}_0^{ABFF}\mathbb{D}_t^{\gamma,\theta,\psi} x - x_0(t) = y(t), \\ {}_0^{ABFF}\mathbb{D}_t^{\gamma,\theta,\psi} y - y_0(t) = -\dfrac{1}{3}\left[x(t) + \left(\dfrac{3}{2}z^2(t) - 1\right)y(t)\right], \quad (x(0), y(0), z(0)) = (1, -1, 2). \\ {}_0^{ABFF}\mathbb{D}_t^{\gamma,\theta,\psi} z - z_0(t) = -y(t) - \dfrac{3}{5}z(t) + y(t)z(t), \end{cases} \tag{18}$$

Let

$$U = \begin{pmatrix} x \\ y \\ z \end{pmatrix}, \qquad F(U) = \begin{pmatrix} y \\ -\dfrac{1}{3}\left[x + \left(\dfrac{3}{2}z^2 - 1\right)y\right] \\ -y - \dfrac{3}{5}z + yz \end{pmatrix}. \tag{19}$$

Then, Eq (18) is

$${}_0^{ABFF}\mathbb{D}_t^{\gamma,\theta,\psi}(U(t) - U_0) = F(U(t)), \qquad U(0) = U_0. \tag{20}$$

3.2. Equivalent weighted Volterra equation

By Proposition 1, the regularized outer-derivative Eq (20) is equivalent to

$${}_0^{ABC}D_t^{\gamma} U(t) = \omega_{\psi,\theta}(t)F(U(t)).$$

Applying the standard AB integral componentwise and using the classical initial value $U(0) = U_0$ yields

$$U(t) = U_0 + a_\gamma \omega_{\psi,\theta}(t)F(U(t)) + b_\gamma \int_0^t (t-s)^{\gamma-1}\omega_{\psi,\theta}(s)F(U(s))\,ds, \tag{21}$$

where

$$a_\gamma = \frac{1-\gamma}{B(\gamma)}, \qquad b_\gamma = \frac{\gamma}{B(\gamma)\Gamma(\gamma)}. \tag{22}$$

Proposition 4. *(Initial compatibility) Let $0 < \gamma < 1$ and suppose that a continuous solution of (21) satisfies the prescribed initial value $U(0) = U_0$. Then necessarily*

$$\omega_{\psi,\theta}(0)F(U_0) = 0. \tag{23}$$

For the present circuit,

$$F(U_0) = \left(-1, \frac{4}{3}, -\frac{11}{5}\right)^T \neq 0,$$

so every fractional circuit computation with the stated non-equilibrium initial condition must use an operational clock for which $\omega_{\psi,\theta}(0) = 0$. The condition is not imposed on the classical limit $\gamma = 1$, where $a_\gamma \to 0$ and the instantaneous AB term disappears.

Proof. Set $t = 0$ in (21). The hereditary integral vanishes and continuity gives

$$U_0 = U_0 + a_\gamma \omega_{\psi,\theta}(0) F(U_0).$$

Because

$$a_\gamma = (1-\gamma)/B(\gamma) > 0$$

for $0 < \gamma < 1$, Eq (23) follows. □

The three scalar equations are therefore

$$x(t) = x_0 + a_\gamma \omega_{\psi,\theta}(t) y(t) + b_\gamma \int_0^t (t-s)^{\gamma-1} \omega_{\psi,\theta}(s) y(s)\, ds, \tag{24}$$

$$y(t) = y_0 - \frac{a_\gamma}{3} \omega_{\psi,\theta}(t) \left[x(t) + \left(\frac{3}{2} z^2(t) - 1 \right) y(t) \right] - \frac{b_\gamma}{3} \int_0^t (t-s)^{\gamma-1} \omega_{\psi,\theta}(s) \left[x(s) + \left(\frac{3}{2} z^2(s) - 1 \right) y(s) \right] ds, \tag{25}$$

$$z(t) = z_0 + a_\gamma \omega_{\psi,\theta}(t) \left[-y(t) - \frac{3}{5} z(t) + y(t) z(t) \right] + b_\gamma \int_0^t (t-s)^{\gamma-1} \omega_{\psi,\theta}(s) \left[-y(s) - \frac{3}{5} z(s) + y(s) z(s) \right] ds. \tag{26}$$

These equations make clear the purpose of the new definition: Every nonlinear element is weighted by the generalized density $\omega_{\psi,\theta}$ before entering the instantaneous and hereditary AB terms. Proposition 4 also shows that the endpoint value of this density is part of the initial-value structure and cannot be chosen independently of U_0.

3.3. Circuit implementation and non-dimensionalization

The algebraic vector field is inherited from the integrator-circuit model of Akgül et al. [14]. Before nondimensionalization, their circuit equations have the form

$$ {}_0^{ABFF}\mathbb{D}_t^{\gamma,\theta,\psi}(X - X_0) = \frac{1}{C_0} \left(-\frac{R_2}{R_1 R_3} \right) Y, \tag{27}$$

$$ {}_0^{ABFF}\mathbb{D}_t^{\gamma,\theta,\psi}(Y - Y_0) = \frac{1}{C_0} \left(\frac{R_7}{R_8 R_5} Y - \frac{1}{R_4} X - \frac{1}{R_6} Z^2 Y \right), \tag{28}$$

$$ {}_0^{ABFF}\mathbb{D}_t^{\gamma,\theta,\psi}(Z - Z_0) = \frac{1}{C_0} \left(\frac{R_{12}}{R_{13} R_9} YZ - \frac{1}{R_{10}} Y - \frac{1}{R_{11}} Z \right). \tag{29}$$

The source article reports $R_1 = R_2 = R_3 = R_5 = R_7 = R_9 = R_{10} = R_{12} = R_{13} = 10\ \text{k}\Omega$, $R_6 = 10.3\ \text{k}\Omega$, $R_4 = 11.62\ \text{k}\Omega$, and $R_{11} = 11.49\ \text{k}\Omega$ [14]. Its printed parameter line also contains "$R_0 = 10.3\ \text{k}\Omega$", whereas the circuit equation uses R_8 and no R_0; we therefore retain that source-level labeling ambiguity rather than infer an unreported value for R_8.

After fixing the resistor ratios, sign conventions of the operational-amplifier stages, and the voltage/time scales, Eqs (27)–(29) reduce to the dimensionless field (19). The generalized derivative changes the constitutive time law of the integrator blocks but not these algebraic gains. Table 1

summarizes the electrical interpretation of the model quantities and clarifies the scope of the present circuit-inspired formulation.

Table 1. Electrical interpretation and scope of the generalized model.

Quantity	Interpretation in the present paper
Reported resistors	Component values above are taken from the reference architecture of Akgül et al. [14]; the nonlinear multiplier stages generate the Z^2Y and YZ products.
C_0	Common integrator capacitance/time-scale parameter before nondimensionalization; no new value is inferred here.
γ	Mittag–Leffler memory order of the AB integrator law.
θ	Fractal exponent entering the operational-time density.
ψ	Phenomenological operational-time map. It is not claimed to be a standalone physical component or a specific resistor/capacitor value.
Hardware/SPICE scope	No new fabricated circuit or SPICE validation is claimed. The revised contribution is mathematical analysis and numerical approximation of a circuit-inspired model; physical calibration of ψ is left for future experimental work.

4. Structural estimates for the nonlinear field

4.1. Equilibrium and Jacobian

The only equilibrium is $U_* = (0, 0, 0)^T$. The Jacobian is

$$J_F(x, y, z) = \begin{pmatrix} 0 & 1 & 0 \\ -\frac{1}{3} & \frac{1}{3} - \frac{1}{2}z^2 & -zy \\ 0 & z - 1 & y - \frac{3}{5} \end{pmatrix}. \tag{30}$$

At the origin,

$$J_F(0, 0, 0) = \begin{pmatrix} 0 & 1 & 0 \\ -1/3 & 1/3 & 0 \\ 0 & -1 & -3/5 \end{pmatrix}.$$

The eigenvalues are $1/6 \pm i\sqrt{11}/6$ and $-3/5$. Hence, the corresponding classical vector field has an unstable oscillatory plane along with a stable dimension. This can be helpful in analyzing the phase diagrams, even though the stability of the nonlocal fractional system cannot be deduced from the classical eigenvalue test alone.

4.2. Growth and Lipschitz bounds

For $\|U\|_\infty \le R$,

$$\begin{aligned} |F_1(U)| &\le R, \\ |F_2(U)| &\le \frac{2}{3}R + \frac{1}{2}R^3, \\ |F_3(U)| &\le \frac{8}{5}R + R^2. \end{aligned}$$

Hence,

$$\|F(U)\|_\infty \le M_F(R) := \max\left\{R, \frac{2}{3}R + \frac{1}{2}R^3, \frac{8}{5}R + R^2\right\}. \tag{31}$$

Using the induced infinity norm of Eq (30), one convenient local Lipschitz constant on the cube $\|U\|_\infty \le R$ is

$$L_F(R) = \max\left\{1, \frac{2}{3} + \frac{3}{2}R^2, \frac{8}{5} + 2R\right\}. \tag{32}$$

Therefore,

$$\|F(U) - F(V)\|_\infty \le L_F(R)\,\|U - V\|_\infty \tag{33}$$

for U, V in that cube.

For later use, define the weighted memory mass

$$H_{\gamma,\omega}(T) = \sup_{0\le t\le T} \int_0^t (t-s)^{\gamma-1}\omega_{\psi,\theta}(s)\,ds. \tag{34}$$

Under Assumption 1,

$$H_{\gamma,\omega}(T) \le \frac{M_\omega T^\gamma}{\gamma}. \tag{35}$$

5. Existence and uniqueness

Let $X = C([0,T];\mathbb{R}^3)$ with norm

$$\|U\|_X = \max_{t\in[0,T]} \|U(t)\|_\infty,$$

and let

$$X_{U_0} = \{U \in X : U(0) = U_0\}, \qquad \mathcal{B}_{R,0} = \{U \in X_{U_0} : \|U\|_X \le R\}.$$

The initial-value-preserving set $\mathcal{B}_{R,0}$ is used below; by Proposition 4, the Volterra operator maps this set into itself at $t = 0$.

Assumption 2. *(Growth and local Lipschitz conditions) On the bounded state cube relevant to $\mathcal{B}_{R,0}$, the vector field is continuous and satisfies*

$$\|F(U)\|_\infty \le C_F\,\|U\|_\infty + M_F, \tag{36}$$

$$\|F(U) - F(V)\|_\infty \le L_F\,\|U - V\|_\infty. \tag{37}$$

For the circuit, explicit choices follow from (31) *and* (32).

Define

$$(\mathcal{A}U)(t) = U_0 + a_\gamma \omega_{\psi,\theta}(t) F(U(t)), \tag{38}$$

$$(\mathcal{K}U)(t) = b_\gamma \int_0^t (t-s)^{\gamma-1}\omega_{\psi,\theta}(s) F(U(s))\,ds. \tag{39}$$

Then a solution is a fixed point of $\mathcal{A} + \mathcal{K}$.

Theorem 1. *(Existence) Assume 1 and 2. Suppose*

$$a_\gamma M_\omega L_F < 1, \tag{40}$$

and there exists $R > 0$ such that

$$\|U_0\|_\infty + \Big(a_\gamma M_\omega + b_\gamma H_{\gamma,\omega}(T)\Big)(C_F R + M_F) \le R. \tag{41}$$

Assume additionally the initial compatibility condition (23)*. Then, problem* (20) *has at least one solution in $\mathcal{B}_{R,0}$.*

Proof. First, Eqs (40) and (37) give

$$\|\mathcal{A}U - \mathcal{A}V\|_X \le a_\gamma M_\omega L_F \|U - V\|_X,$$

so $\mathcal{A}$ is a contraction. Next, Eq (36) implies

$$\|\mathcal{K}U(t)\|_\infty \le b_\gamma (C_F R + M_F) H_{\gamma,\omega}(T),$$

so $\mathcal{K}$ maps bounded sets into bounded sets. Continuity follows from dominated convergence.

To prove compactness, set $M_R = C_F R + M_F$ and take $U \in \mathcal{B}_{R,0}$. For $0 \le t_1 < t_2 \le T$, split the history difference as

$$\begin{aligned}(\mathcal{K}U)(t_2) - (\mathcal{K}U)(t_1) = b_\gamma \int_0^{t_1} \Big[(t_2 - s)^{\gamma-1} - (t_1 - s)^{\gamma-1}\Big] \omega_{\psi,\theta}(s) F(U(s))\, ds \\ + b_\gamma \int_{t_1}^{t_2} (t_2 - s)^{\gamma-1} \omega_{\psi,\theta}(s) F(U(s))\, ds.\end{aligned}$$

Consequently,

$$\|(\mathcal{K}U)(t_2) - (\mathcal{K}U)(t_1)\|_\infty \le b_\gamma M_R M_\omega \int_0^{t_1} \Big|(t_2 - s)^{\gamma-1} - (t_1 - s)^{\gamma-1}\Big|\, ds + \frac{b_\gamma M_R M_\omega}{\gamma}(t_2 - t_1)^\gamma.$$

The second term converges to zero uniformly as $t_2 - t_1 \to 0$. The first term also converges uniformly to zero because translations of the integrable kernel $r^{\gamma-1}$ are continuous in $L^1(0, T)$. Thus, $\mathcal{K}(\mathcal{B}_{R,0})$ is equicontinuous. Together with the uniform bound above, the Arzelà–Ascoli theorem shows that $\mathcal{K}$ maps bounded sets into relatively compact sets; hence, $\mathcal{K}$ is compact.

Finally, for $U, V \in \mathcal{B}_{R,0}$,

$$\|\mathcal{A}U + \mathcal{K}V\|_X \le \|U_0\|_\infty + \Big(a_\gamma M_\omega + b_\gamma H_{\gamma,\omega}(T)\Big)(C_F R + M_F) \le R.$$

The compatibility condition gives $(\mathcal{A}U + \mathcal{K}V)(0) = U_0$. Krasnosel'skii's fixed-point theorem therefore provides a fixed point of $\mathcal{A} + \mathcal{K}$ in $\mathcal{B}_{R,0}$. □

Remark 2. *The original circuit article used a Schauder-style argument for the full AB integral operator. Because the AB integral contains an instantaneous Nemytskii term, compactness of the full operator is not automatic. The splitting above preserves the same existence objective while treating the local term as a contraction and the history term as a compact Volterra operator.*

Theorem 2. *Assume that two solutions U, V remain in a cube on which the Lipschitz constant is L_F, and set*

$$\eta = a_\gamma M_\omega L_F. \tag{42}$$

If $\eta < 1$, then the two solutions coincide on every finite interval on which they both exist and remain in that cube.

Proof. Let $d(t) = \|U(t) - V(t)\|_\infty$. Subtracting the two Volterra equations gives

$$d(t) \le \eta d(t) + b_\gamma M_\omega L_F \int_0^t (t-s)^{\gamma-1} d(s)\, ds.$$

Because $\eta < 1$,

$$d(t) \le c_\gamma \int_0^t (t-s)^{\gamma-1} d(s)\, ds, \qquad c_\gamma = \frac{b_\gamma M_\omega L_F}{1-\eta}.$$

The fractional Gronwall inequality with zero free term yields $d(t) = 0$ on $[0, T]$. Unlike the former condition $L_F(a_\gamma M_\omega + b_\gamma H_{\gamma,\omega}(T)) < 1$, condition (42) does not grow with the final time. □

Theorem 3. *(Continuous dependence on the initial state) Under the hypotheses of Theorem 2, solutions with initial states U_0 and $\widetilde{U}_0$ satisfy, for $0 \le t \le T$,*

$$\|U(t) - \widetilde{U}(t)\|_\infty \le \frac{\|U_0 - \widetilde{U}_0\|_\infty}{1-\eta} E_\gamma\!\left(\frac{b_\gamma M_\omega L_F \Gamma(\gamma)}{1-\eta} t^\gamma\right). \tag{43}$$

Proof. With $d(t) = \|U(t) - \widetilde{U}(t)\|_\infty$, subtraction gives

$$d(t) \le \Delta_0 + \eta d(t) + b_\gamma M_\omega L_F \int_0^t (t-s)^{\gamma-1} d(s)\, ds, \quad \Delta_0 = \|U_0 - \widetilde{U}_0\|_\infty.$$

Rearrangement followed by the standard fractional Gronwall inequality proves (43). □

Proposition 5. *(Continuation criterion) Suppose Assumptions 1 and 2 hold locally on bounded cubes and $\eta < 1$ on each cube reached by a solution. A local solution can be continued beyond any time T_0 provided its norm remains bounded on $[0, T_0]$ and the density remains bounded there. Consequently, a finite maximal existence time can occur only together with loss of the bounded-set hypotheses (in particular, unbounded state norm or density).*

Proof. At T_0, split the Volterra history into the already known integral over $[0, T_0]$ and the new integral over $[T_0, t]$. The first part is a continuous known forcing. For a suitably small interval $[T_0, T_0 + \delta]$, the Krasnosel'skii decomposition used in Theorem 1 can be used on a cube that contains the bounded trace at T_0; the hereditary term for the new interval is $O(\delta^\gamma)$. Because of the uniqueness of Theorem 2, the extensions are compatible where they coincide. Repeating produces continuation as long as the bounded-set properties hold. □

Remark 3. *The long-time runs in Section 8 are not justified by a horizon-dependent contraction factor. Their computed states remain inside $[-2, 2]^3$ for the reported parameter sets. On this cube, we obtain $L_F(2) = 20/3$. For example, with $\psi(t) = \psi_b(t) = t^2/(1+t)$, $M_\omega < 1$, and $\gamma = 0.90$, condition (42) gives $\eta < 0.708$; for the other reported γ values with the base clock, the instantaneous factor is smaller.*

Across the complete reported fractional parameter set, the largest value occurs for the exponential scale-function case at $\gamma = 0.95$, for which $M_\omega \approx 2.69124$ on $[0, 100]$ and $\eta \approx 0.92384 < 1$. Thus, all reported fractional runs satisfy the uniqueness/stability smallness condition on the numerically observed cube, while Proposition 5 states separately the analytical boundedness requirement needed for rigorous continuation to a prescribed horizon.

6. Ulam–Hyers stability

Definition 4. *(Ulam–Hyers stability) Problem* (20) *is Ulam–Hyers stable on* $[0, T]$ *if there exists* $C_{UH} > 0$ *such that every V satisfying*

$$\left\| {}^{ABFF}_{0}\mathbb{D}_t^{\gamma,\theta,\psi}(V(t) - V(0)) - F(V(t)) \right\|_\infty \le \varepsilon \tag{44}$$

is within $C_{UH}\varepsilon$ *of the exact solution having the same initial state.*

Let

$$P_T = M_\omega \left(a_\gamma + \frac{b_\gamma T^\gamma}{\gamma} \right), \qquad \eta = a_\gamma M_\omega L_F < 1. \tag{45}$$

Lemma 1. *(Integral form of a perturbed solution) If* (44) *holds, there exists* $e \in C([0, T]; \mathbb{R}^3)$ *with* $\|e(t)\|_\infty \le \varepsilon$ *such that*

$$\begin{aligned} V(t) = V(0) &+ a_\gamma \omega_{\psi,\theta}(t) F(V(t)) + b_\gamma \int_0^t (t - s)^{\gamma-1} \omega_{\psi,\theta}(s) F(V(s))\, ds \\ &+ a_\gamma \omega_{\psi,\theta}(t) e(t) + b_\gamma \int_0^t (t - s)^{\gamma-1} \omega_{\psi,\theta}(s) e(s)\, ds. \end{aligned} \tag{46}$$

The perturbation line is bounded by $P_T\varepsilon$.

Theorem 4. *(Ulam–Hyers stability on an arbitrary finite horizon) If* $\eta < 1$, *then problem* (20) *is Ulam–Hyers stable with*

$$C_{UH}(T) = \frac{P_T}{1 - \eta} E_\gamma\left(\frac{b_\gamma M_\omega L_F \Gamma(\gamma)}{1 - \eta} T^\gamma \right). \tag{47}$$

No condition of the form $q(T) < 1$ *is required.*

Proof. Let U be the exact solution with $U(0) = V(0)$ and put $d(t) = \|V(t) - U(t)\|_\infty$. Lemma 1 and local Lipschitz continuity give

$$d(t) \le P_T\varepsilon + \eta d(t) + b_\gamma M_\omega L_F \int_0^t (t - s)^{\gamma-1} d(s)\, ds.$$

After dividing by $1 - \eta$, the fractional Gronwall inequality yields (47). □

Generalized Ulam–Hyers–Rassias stability. Let φ: $[0, T] \to (0, \infty)$ be continuous and introduce the weighted norm

$$\|W\|_\varphi = \sup_{0 \le t \le T} \frac{\|W(t)\|_\infty}{\varphi(t)}. \tag{48}$$

Assume

$$\int_0^t (t-s)^{\gamma-1}\omega_{\psi,\theta}(s)\varphi(s)\,ds \le \Lambda_\varphi \varphi(t), \quad 0 \le t \le T, \tag{49}$$

and define

$$q_\varphi = L_F\left(a_\gamma M_\omega + b_\gamma \Lambda_\varphi\right). \tag{50}$$

If $q_\varphi < 1$ and the residual in (44) is bounded by $\varepsilon\varphi(t)$, then

$$\|V(t) - U(t)\|_\infty \le \frac{a_\gamma M_\omega + b_\gamma \Lambda_\varphi}{1 - q_\varphi}\,\varepsilon\varphi(t). \tag{51}$$

Indeed, division of the pointwise difference inequality by $\varphi(t)$ and use of (49) give

$$\|V - U\|_\varphi \le (a_\gamma M_\omega + b_\gamma \Lambda_\varphi)\varepsilon + q_\varphi \|V - U\|_\varphi,$$

which proves (51). This weighted formulation avoids the unjustified replacement of a pointwise $\varphi(t)$ bound by the unweighted constant used in the previous version.

7. Numerical approximation

This section gives a self-contained derivation of the numerical method used in the simulations. It discretizes the Volterra equation obtained from the regularized ABFF model

$$ {}_0^{ABFF}\mathbb{D}_t^{\gamma,\theta,\psi}(U - U_0) = F(U).$$

The numerical source is therefore multiplied by the generalized ψ-fractal density.

7.1. Weighted source and grid notation

Define

$$G(t, U) = \omega_{\psi,\theta}(t)F(U). \tag{52}$$

The Volterra Eq (21) can then be written as

$$U(t) = U_0 + a_\gamma G(t, U(t)) + b_\gamma \int_0^t (t-s)^{\gamma-1} G(s, U(s))\,ds, \tag{53}$$

where a_γ and b_γ are defined in (22). Let

$$t_n = nh, \qquad h = \frac{T}{N}, \qquad n = 0, 1, \ldots, N, \tag{54}$$

and denote

$$U_n \approx U(t_n), \qquad G_n = G(t_n, U_n) = \omega_{\psi,\theta}(t_n)F(U_n).$$

The term $a_\gamma G(t, U(t))$ in (53) is instantaneous and nonlinear. To retain the explicit character of the method used in the original circuit study, it is evaluated at the preceding time level:

$$G(t_{n+1}, U(t_{n+1})) \approx G_n. \tag{55}$$

This lagging is the only first-order part of the construction. An implicit corrector could instead solve

$$U_{n+1} = U_0 + a_\gamma G(t_{n+1}, U_{n+1}) + H_{n+1}.$$

7.2. Two-step extrapolation of the history source

On the cell $[t_j, t_{j+1}]$, the source is approximated by the linear polynomial through the two already available values G_{j-1} and G_j:

$$P_j(s) = \frac{s - t_{j-1}}{h} G_j - \frac{s - t_j}{h} G_{j-1}, \qquad s \in [t_j, t_{j+1}]. \tag{56}$$

Although (56) is obtained from the Lagrange formula, it is an extrapolation over the current cell because both data values lie at or before t_j. For $j = 0$, there is no value G_{-1}; we therefore set

$$G_{-1} = G_0, \tag{57}$$

so that $P_0(s) = G_0$. This gives a one-step product-Euler start and permits the same two-step recurrence to be used for all subsequent steps.

Evaluating (53) at t_{n+1}, applying (55), splitting the history integral over the mesh cells, and inserting (56) yields

$$U_{n+1} = U_0 + a_\gamma G_n + b_\gamma \sum_{j=0}^{n} \int_{t_j}^{t_{j+1}} (t_{n+1} - s)^{\gamma-1} P_j(s)\, ds. \tag{58}$$

7.3. Analytical derivation of the convolution weights

The weights are now derived in the main text. Set $m = n - j$ and use the local variable $s = t_j + h\xi$ and $0 \le \xi \le 1$. Then,

$$t_{n+1} - s = h(m + 1 - \xi), \qquad P_j(t_j + h\xi) = (1 + \xi)G_j - \xi G_{j-1}.$$

Therefore,

$$\begin{aligned} \int_{t_j}^{t_{j+1}} (t_{n+1} - s)^{\gamma-1} P_j(s)\, ds =& h^\gamma \left[\int_0^1 (m + 1 - \xi)^{\gamma-1} (1 + \xi)\, d\xi \right] G_j \\ & - h^\gamma \left[\int_0^1 (m + 1 - \xi)^{\gamma-1} \xi\, d\xi \right] G_{j-1}. \end{aligned} \tag{59}$$

We get

$$\int_0^1 (m + 1 - \xi)^{\gamma-1} (1 + \xi)\, d\xi = \frac{A_{n,j}^{(\gamma)}}{\gamma(\gamma + 1)}, \tag{60}$$

$$\int_0^1 (m + 1 - \xi)^{\gamma-1} \xi\, d\xi = \frac{C_{n,j}^{(\gamma)}}{\gamma(\gamma + 1)}, \tag{61}$$

where

$$A_{n,j}^{(\gamma)} = (n + 1 - j)^\gamma (n - j + 2 + \gamma) - (n - j)^\gamma (n - j + 2 + 2\gamma), \tag{62}$$

$$C_{n,j}^{(\gamma)} = (n + 1 - j)^{\gamma+1} - (n - j)^\gamma (n - j + 1 + \gamma). \tag{63}$$

Terms of the form 0^γ are understood as zero. Since

$$\Gamma(\gamma+2) = \gamma(\gamma+1)\Gamma(\gamma),$$

substituting (60) and (61) into (58) gives the explicit recurrence

$$U_{n+1} = U_0 + a_\gamma G_n + \kappa_{\gamma,h} \sum_{j=0}^{n} \left(A_{n,j}^{(\gamma)} G_j - C_{n,j}^{(\gamma)} G_{j-1} \right) \tag{64}$$

with

$$\kappa_{\gamma,h} = \frac{\gamma h^\gamma}{B(\gamma)\Gamma(\gamma+2)}. \tag{65}$$

7.4. First step and componentwise recurrence

For $n = 0$, relation (57) reduces (64) to

$$U_1 = U_0 + \left(a_\gamma + \frac{h^\gamma}{B(\gamma)\Gamma(\gamma)} \right) G_0. \tag{66}$$

Thus the starting value does not require a separate nonlinear solver. For the circuit, define

$$G_{x,n} = \widehat{\omega}_n y_n, \tag{67}$$

$$G_{y,n} = -\frac{\widehat{\omega}_n}{3} \left[x_n + \left(\frac{3}{2} z_n^2 - 1 \right) y_n \right], \tag{68}$$

$$G_{z,n} = \widehat{\omega}_n \left(-y_n - \frac{3}{5} z_n + y_n z_n \right), \tag{69}$$

where, in the revised algorithm,

$$\widehat{\omega}_n = \omega_{\psi,\theta}(t_n)$$

is evaluated directly under Assumption 1. Reported computations do not replace an unbounded endpoint by a mesh-dependent midpoint value. The three components of (64) are

$$x_{n+1} = x_0 + a_\gamma G_{x,n} + \kappa_{\gamma,h} \sum_{j=0}^{n} \left(A_{n,j}^{(\gamma)} G_{x,j} - C_{n,j}^{(\gamma)} G_{x,j-1} \right), \tag{70}$$

$$y_{n+1} = y_0 + a_\gamma G_{y,n} + \kappa_{\gamma,h} \sum_{j=0}^{n} \left(A_{n,j}^{(\gamma)} G_{y,j} - C_{n,j}^{(\gamma)} G_{y,j-1} \right), \tag{71}$$

$$z_{n+1} = z_0 + a_\gamma G_{z,n} + \kappa_{\gamma,h} \sum_{j=0}^{n} \left(A_{n,j}^{(\gamma)} G_{z,j} - C_{n,j}^{(\gamma)} G_{z,j-1} \right). \tag{72}$$

Here, $G_{\ell,-1} = G_{\ell,0}$ for $\ell \in \{x, y, z\}$.

7.5. Endpoint compatibility and algorithm

The instantaneous AB operator involves $\omega_{\psi,\theta}(t_n)$ directly, rather than in terms of its integral. As such, an adjustment of an infinite $\omega_{\psi,\theta}(0)$ to a mesh-based finite value affects the discrete problem formulation. Thus, the adjusted version of the implementation requires a finite end point evaluation and, if $0 < \gamma < 1$, additionally verifies the compatibility criterion $\omega_{\psi,\theta}(0)F(U_0) = 0$. In case of failing any of the conditions, the program aborts with a warning, and the respective example is not considered in the circuit results. In the bounded clock case (17), the value at the end point can be found analytically and is equal to zero (see Algorithm 1).

Algorithm 1 Explicit ABFF product-integration method.

Require: T, N, γ, θ, ψ and U_0
Ensure: Approximations $U_n \approx U(t_n)$ for $n = 0, \ldots, N$
1: $h \leftarrow T/N$; construct $t_n = nh$
2: Compute $B(\gamma)$, a_γ, and $\kappa_{\gamma,h}$
3: Evaluate $\omega_{\psi,\theta}(t_n)$; verify finiteness and, for $0 < \gamma < 1$, verify $\omega_{\psi,\theta}(0)F(U_0) = 0$
4: $G_0 \leftarrow \omega_{\psi,\theta}(0)F(U_0)$ and set $G_{-1} \leftarrow G_0$
5: **for** $n = 0, 1, \ldots, N-1$ **do**
6: $\quad H \leftarrow 0 \in \mathbb{R}^3$
7: $\quad$ **for** $j = 0, 1, \ldots, n$ **do**
8: $\quad\quad$ Compute $A_{n,j}^{(\gamma)}$ and $C_{n,j}^{(\gamma)}$ from (62)–(63)
9: $\quad\quad H \leftarrow H + A_{n,j}^{(\gamma)} G_j - C_{n,j}^{(\gamma)} G_{j-1}$
10: $\quad$ **end for**
11: $\quad U_{n+1} \leftarrow U_0 + a_\gamma G_n + \kappa_{\gamma,h} H$
12: $\quad G_{n+1} \leftarrow \omega_{\psi,\theta}(t_{n+1})F(U_{n+1})$
13: **end for**

7.6. Integer-order reduction

Proposition 6. *If $\gamma = \theta = 1$ and $\psi(t) = t$, then $a_\gamma = 0$, $\omega_{\psi,\theta}(t) = 1$, and the difference of two consecutive forms of* (64) *is the two-step Adams–Bashforth method after the starting step:*

$$U_{n+1} = U_n + h\left(\frac{3}{2}F(U_n) - \frac{1}{2}F(U_{n-1})\right), \qquad n \geq 1. \tag{73}$$

Proof. Since $\gamma = 1$, we have $B(1) = 1$, $A_{n,j}^{(1)} = 3$, and $C_{n,j}^{(1)} = 1$. Subtracting the formula for U_n from that for U_{n+1} cancels all common history contributions and leaves (73). The convention $G_{-1} = G_0$ provides the first explicit Euler step. □

7.7. Consistency and convergence

Let $g(t) = G(t, U(t))$ be the exact weighted source and define the nodal defect by inserting the exact grid values into (64):

$$\delta_{n+1} = U(t_{n+1}) - U_0 - a_\gamma g(t_n) - \kappa_{\gamma,h} \sum_{j=0}^{n} \left(A_{n,j}^{(\gamma)} g(t_j) - C_{n,j}^{(\gamma)} g(t_{j-1})\right), \tag{74}$$

where $g(t_{-1}) = g(t_0)$.

Proposition 7. *(Consistency) Assume $g \in C^2([0,T];\mathbb{R}^3)$ and a bounded endpoint density. Then*

$$\max_{0\le n\le N-1} \|\delta_{n+1}\|_\infty \le C_1 h + C_2 h^{1+\gamma} + C_3 h^2, \tag{75}$$

with constants independent of h; hence, the explicit method is first-order consistent for $0 < \gamma < 1$.

Proof. The lagged instantaneous term contributes

$$a_\gamma \|g(t_{n+1}) - g(t_n)\|_\infty \le a_\gamma \|g'\|_\infty h.$$

On cells $j \ge 1$, the two-step extrapolation remainder is $O(h^2)$, and convolution with the integrable kernel preserves that order on a fixed interval. The constant first-cell start contributes $O(h^{1+\gamma})$. Summation gives (75). □

The integral representations of the product-integration weights imply $A^{(\gamma)}_{n,j}, C^{(\gamma)}_{n,j} \ge 0$. Moreover, with $m = n - j$, one has the uniform estimate

$$A^{(\gamma)}_{n,j} + C^{(\gamma)}_{n,j} \le 4(m+1)^{\gamma-1}, \qquad 0 < \gamma \le 1. \tag{76}$$

This estimate follows directly by factoring the cell-integral formulas (60) and (61) and using the monotonicity of $r^{\gamma-1}$ on each grid cell.

Lemma 2. *(Discrete weakly singular stability) Let $0 < \gamma < 1$, $0 \le \eta < 1$, and let a nonnegative sequence satisfy $e_0 = 0$ and*

$$e_{n+1} \le \eta e_n + \lambda h^\gamma \sum_{j=0}^{n} (n-j+1)^{\gamma-1} \max\{e_j, e_{j-1}\} + \rho_h, \tag{77}$$

with $e_{-1} = e_0$ and $t_n \le T$. Then there is a constant C_T, independent of h and N, such that $\max_{0\le n\le N} e_n \le C_T \rho_h$.

Proof. Iteration of the one-step term ηe_n yields a resolvent with geometrically weighted weights. Convolution of this resolvent with the kernel $(m+1)^{\gamma-1}$ is bounded above by $C_{\eta,\gamma}(m+1)^{\gamma-1}$; this can be done by splitting the geometric sum at $m/2$ and using the estimates

$$(m - r + 1)^{\gamma-1} \le 2^{1-\gamma}(m+1)^{\gamma-1}$$

in the first half of the sum and exponential decay of η^r in the other half. The estimate (77) thus reduces to a standard discrete weakly singular Volterra estimate. The resolvent series obtained by successive substitutions has the kth term estimated by $C^k t_n^{k\gamma}/\Gamma(k\gamma+1)$ (the discrete convolution sum is bounded by the corresponding beta-integral up to a γ-dependent constant). The series is dominated by a Mittag–Leffler function on $[0,T]$, yielding $e_n \le C_T \rho_h$ uniformly in the mesh. □

Theorem 5. *(Global first-order convergence) Assume the exact solution satisfies $\|U(t)\|_\infty \le R$ on $[0,T]$, $g \in C^2([0,T];\mathbb{R}^3)$, and Assumption 1 holds. Suppose there exists $R_* > R$ such that*

$$\eta_* = a_\gamma M_\omega L_F(R_*) < 1. \tag{78}$$

Then there exist $h_0 > 0$ and $C_T > 0$, independent of h, such that for every $0 < h \le h_0$, the numerical solution is well defined, remains in the cube $\|U_n\|_\infty < R_*$, and

$$\max_{0\le n\le N} \|U(t_n) - U_n\|_\infty \le C_T h. \tag{79}$$

Proof. Set $d_* = R_* - R > 0$ and let $E_n = \|U(t_n) - U_n\|_\infty$. As long as the numerical states remain in the R_*-cube,

$$\|G(t_j, U(t_j)) - G(t_j, U_j)\|_\infty \le M_\omega L_F(R_*) E_j.$$

Subtracting the numerical scheme from the exact defect identity and using (76) gives, on every such truncated interval,

$$E_{n+1} \le \eta_* E_n + Ch^\gamma \sum_{j=0}^{n} (n - j + 1)^{\gamma-1} \max\{E_j, E_{j-1}\} + \|\delta_{n+1}\|_\infty.$$

Proposition 7 gives

$$\rho_h := \max_n \|\delta_{n+1}\|_\infty \le C_0 h,$$

so Lemma 2, applied to any truncated sequence, yields $E_n \le C_T h$ with the same mesh-independent constant C_T.

It remains to justify that the numerical states do not leave the R_*-cube. If a first exit index existed, then all preceding states would lie in the cube, and the truncated estimate above would apply through that index. Choose

$$h_0 < \frac{d_*}{2C_T}.$$

For $h \le h_0$, we would have

$$\|U_n\|_\infty \le \|U(t_n)\|_\infty + E_n \le R + C_T h < R_*$$

at the alleged first exit, a contradiction. Hence, no exit occurs, the local Lipschitz estimate is valid on the whole grid, and the global first-order bound follows. □

The direct history sum takes $O(N^2)$ work and $O(N)$ space. The provided MATLAB program reproduces the reported circuit figures and tables, rejects a non-finite endpoint density, and also stops if the fractional circuit data violate $\omega_{\psi,\theta}(0)F(U_0) = 0$. The convergence theorem assumes the additional smoothness $g \in C^2$; the exact benchmark below is used specifically to verify that theorem.

8. Numerical results and simulations

Unless stated otherwise, $U_0 = (1, -1, 2)^T$, $T = 100$, and the fractional circuit simulations use $N = 1800$ ($h = 0.05556$). In accordance with Proposition 4, every reported run with $0 < \gamma < 1$ satisfies $\omega_{\psi,\theta}(0)F(U_0) = 0$. To summarize oscillatory trajectories, we discard the initial transient $0 \le t < 10$ and report the component amplitude

$$A_q = \frac{1}{2}\left(\max_{10 \le t_n \le T} q_n - \min_{10 \le t_n \le T} q_n\right), \qquad q \in \{x, y, z\}, \tag{80}$$

and P_x, the median separation of successive detected local maxima of $x(t)$. These quantities are more informative for an oscillatory system than the terminal state. The previous column $\max_n \|U_n\|_2$ is removed because it was always attained at the initial state and therefore contained no parameter-dependent information.

8.1. *Classical integer-order reference*

For $\gamma = \theta = 1$ and $\psi(t) = t$, the limiting regularized equation is the ordinary first-order system. Figure 1 is generated with MATLAB's adaptive `ode45` using 4000 output points, relative tolerance 10^{-9}, and absolute tolerance 10^{-11}.

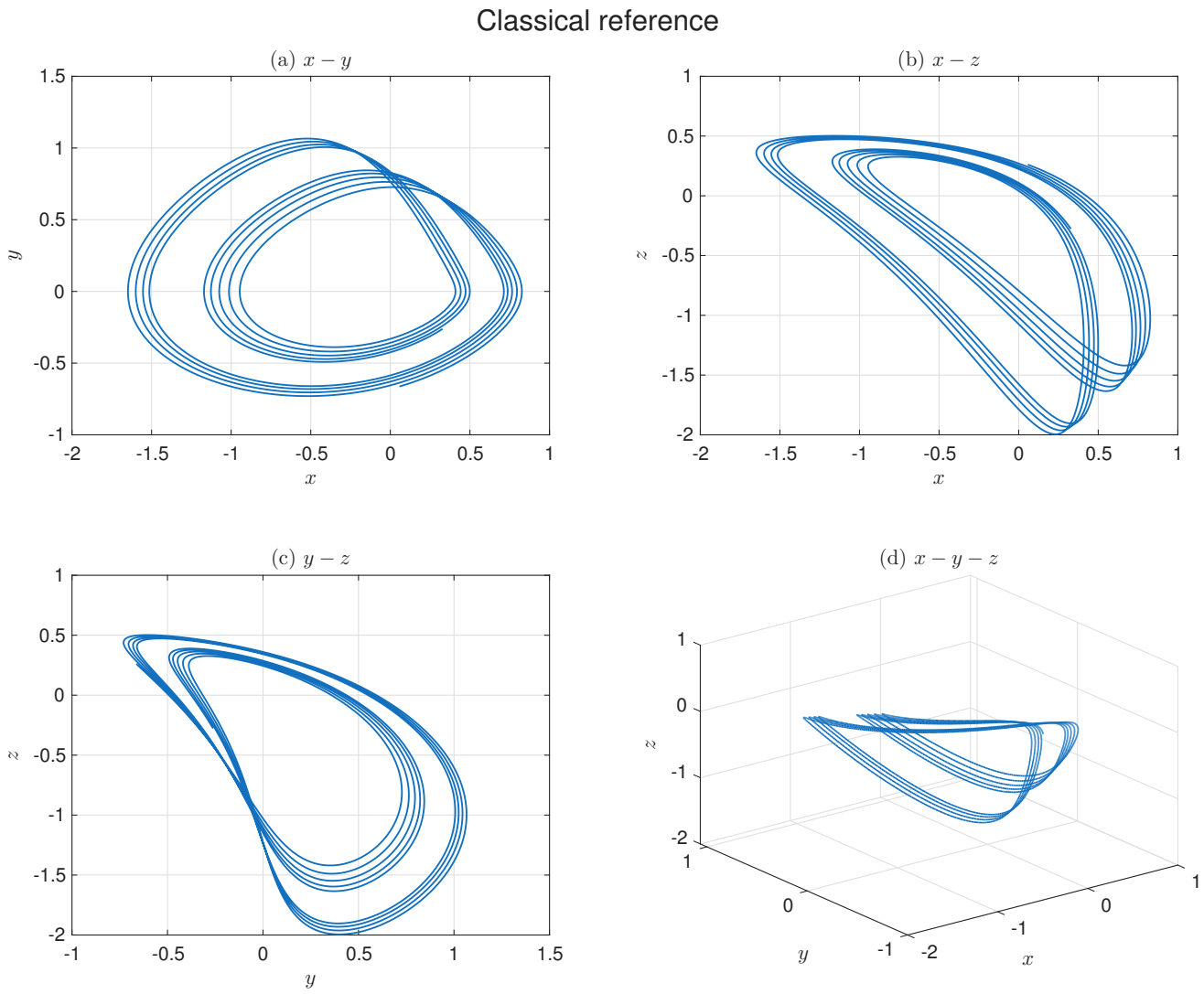

Figure 1. Classical reference trajectory for $U_0 = (1, -1, 2)^T$, $T = 100$, $\gamma = \theta = 1$, and $\psi(t) = t$. Panels show the x–y, x–z, y–z, and three-dimensional phase projections. The trajectory is computed with `ode45` (4000 output points, RelTol = 10^{-9}, AbsTol = 10^{-11}).

8.2. *Fractional AB attractor*

Figure 2 uses $\gamma = 0.90$, $\theta = 1$, and the compatible base clock

$$\psi_b(t) = t^2/(1 + t)$$

from (17), for which $\omega_{\psi,\theta}(0) = 0$. This example illustrates a fractional ABFF trajectory satisfying the same endpoint assumptions used in the analysis. Because Figure 1 uses the identity clock, the

two figures should not be interpreted as a one-parameter memory-only comparison; the effect of γ is isolated next by keeping ψ_b fixed.

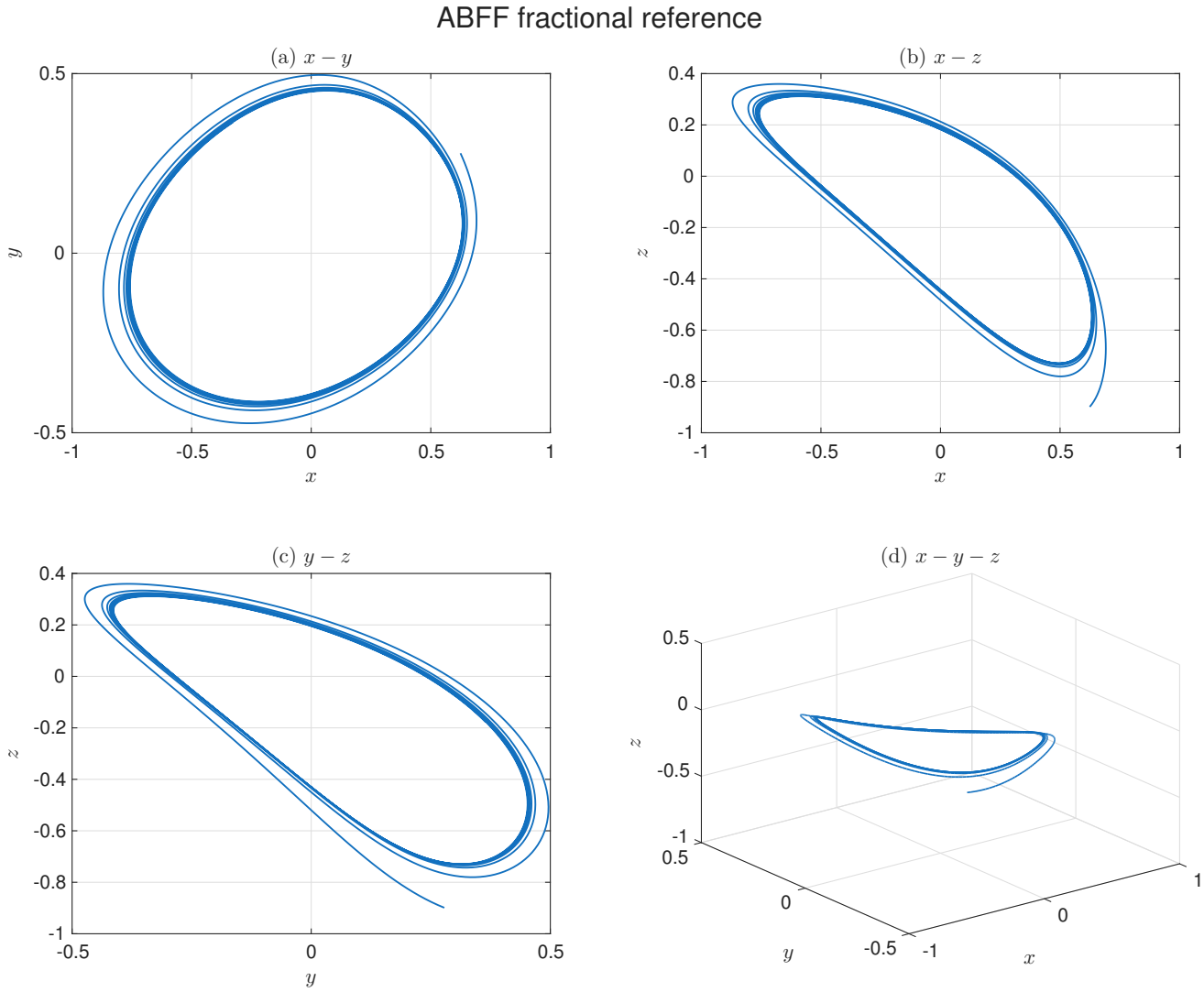

Figure 2. Endpoint-compatible ABFF phase portraits for $U_0 = (1, -1, 2)^T$, $T = 100$, $N = 1800$ ($h = 0.05556$), $\gamma = 0.90$, $\theta = 1$, and $\psi(t) = t^2/(1 + t)$. The same four phase projections as in Figure 1 are shown.

8.3. Influence of the fractional order

We fix $\theta = 1$ and the endpoint-compatible clock

$$\psi(t) = \psi_b(t) = t^2/(1 + t)$$

and vary $\gamma \in \{0.99, 0.98, 0.97, 0.965\}$. Figures 3–5 show the time histories, and Table 2 quantifies the post-transient oscillation rather than comparing only $U(T)$.

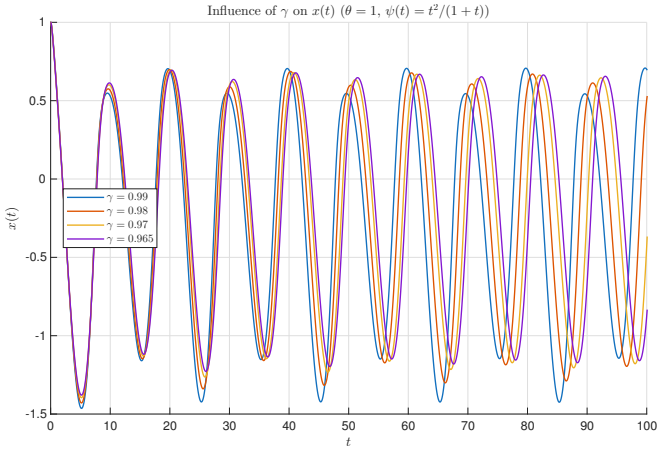

Figure 3. $x(t)$ for $T = 100$, $N = 1800$, $\theta = 1$, $\psi(t) = t^2/(1+t)$, and $\gamma = 0.99, 0.98, 0.97, 0.965$.

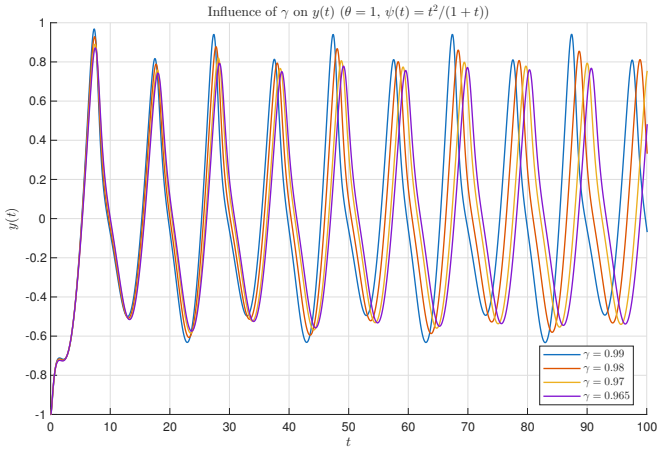

Figure 4. $y(t)$ for the same grid and parameters as Figure 3.

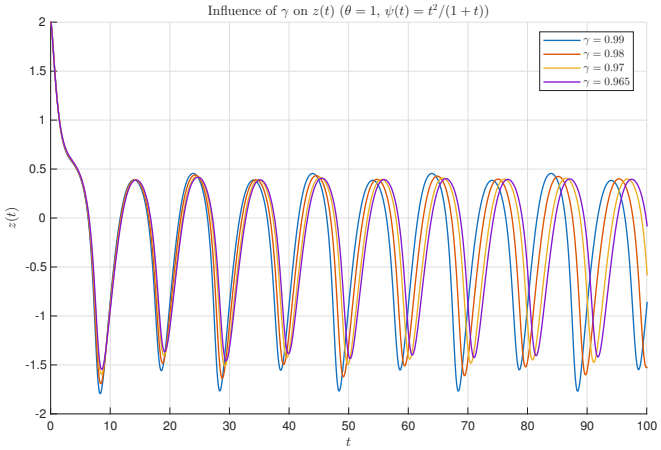

Figure 5. $z(t)$ for the same grid and parameters as Figure 3.

Table 2. Post-transient amplitudes and median x-period for different fractional orders ($t \in [10, 100]$, $N = 1800$, $\theta = 1$, $\psi(t) = t^2/(1 + t)$).

γ	A_x	A_y	A_z	P_x
0.990	1.06634	0.78732	1.11196	10.0000
0.980	1.01865	0.74245	1.03741	10.1111
0.970	0.97927	0.70250	0.96921	10.2778
0.965	0.96126	0.68361	0.93675	10.3889

In the fractional-order case, the decrease of γ from 0.99 to 0.965 is reflected by the following damping of the amplitude: A_x, A_y, and A_z are reduced by about 9.9%, 13.2%, and 15.8%, while the median value of x-period is increased only from 10.0000 to 10.3889. Thus, in this compatible-clock family, decreasing γ primarily reduces the oscillation amplitudes while producing a more modest period elongation.

8.4. Influence of the fractal exponent under the bounded-density hypothesis

To isolate θ without violating Assumption 1, we fix $\gamma = 0.99$ and use the bounded clock (17). The density behaves like $2\theta t^{2\theta-1}$ near zero and is finite for every reported θ. No first-cell midpoint regularization is used. Figures 6–8 show the component histories for the reported fractal exponents, while Table 3 summarizes the corresponding post-transient amplitudes and median x-period.

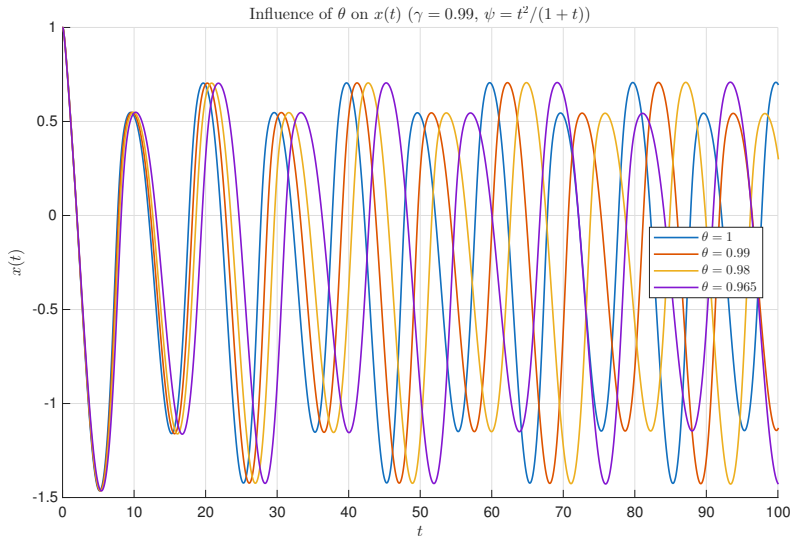

Figure 6. $x(t)$ for $T = 100$, $N = 1800$, $\gamma = 0.99$, $\psi(t) = t^2/(1+t)$, and $\theta = 1, 0.99, 0.98, 0.965$.

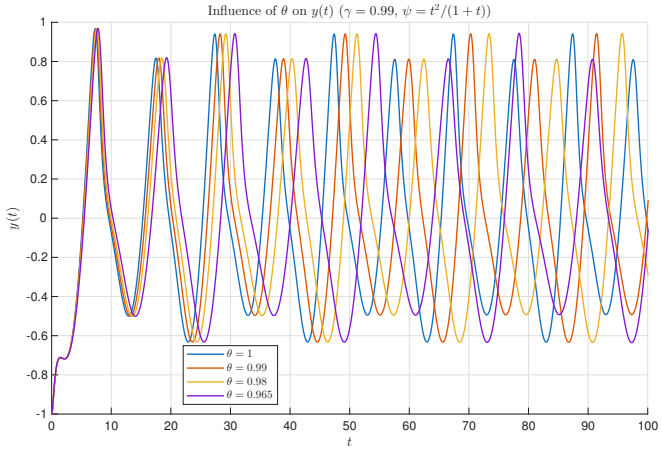

Figure 7. $y(t)$ for the same bounded-density grid and parameters as Figure 6.

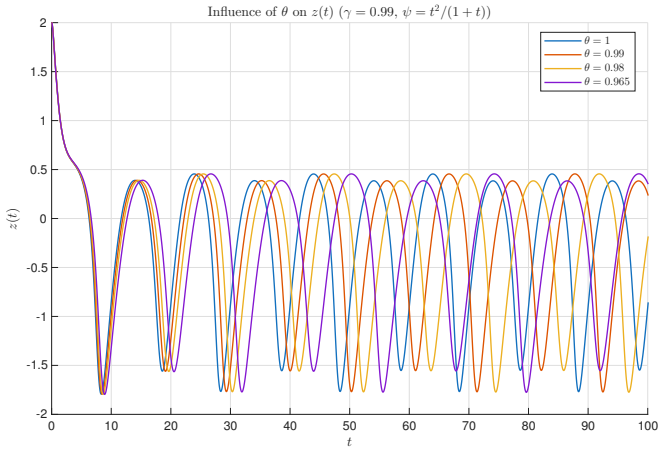

Figure 8. $z(t)$ for the same bounded-density grid and parameters as Figure 6.

Table 3. Post-transient amplitudes and median x-period for the bounded-density fractal-exponent study ($t \in [10, 100]$, $N = 1800$, $\gamma = 0.99$, $\psi(t) = t^2/(1 + t)$).

θ	A_x	A_y	A_z	P_x
1.000	1.06634	0.78732	1.11196	10.0000
0.990	1.06704	0.78818	1.11324	10.4444
0.980	1.06817	0.78893	1.11468	11.0556
0.965	1.06876	0.78957	1.11567	11.8889

The principal effect in this bounded family is a change in oscillation period: as θ decreases from 1 to 0.965, P_x increases from 10.0000 to 11.8889 (about 18.9%), while all three amplitudes change by less than 0.4%. This is precisely why period-based diagnostics are preferable to terminal coordinates for the fractal-exponent sensitivity study.

8.5. Study of the scale function ψ

We fix $\gamma = 0.95$, $\theta = 1$ and write $q(t) = t^2/(1+t)$. To vary the operational clock while preserving the initial compatibility condition, we compare

$$\psi_1(t) = q(t), \quad \psi_2(t) = q(t) + 0.005q^2(t), \quad \psi_3(t) = \frac{\log(1 + 0.05q(t))}{0.05}, \quad \psi_4(t) = \frac{e^{0.01q(t)} - 1}{0.01}.$$

All four functions are increasing for $t > 0$, satisfy $\psi_i(0) = 0$ and $\psi_i'(0) = 0$, and hence have bounded endpoint-compatible densities $\omega_{\psi_i,1}(0) = 0$. They are mathematical sensitivity profiles for slower or faster operational clocks; no direct hardware realization of these analytic forms is claimed.

Figures 9–11 compare the resulting trajectories, x-responses, and operational-time densities, while Table 4 reports the associated post-transient oscillation statistics.

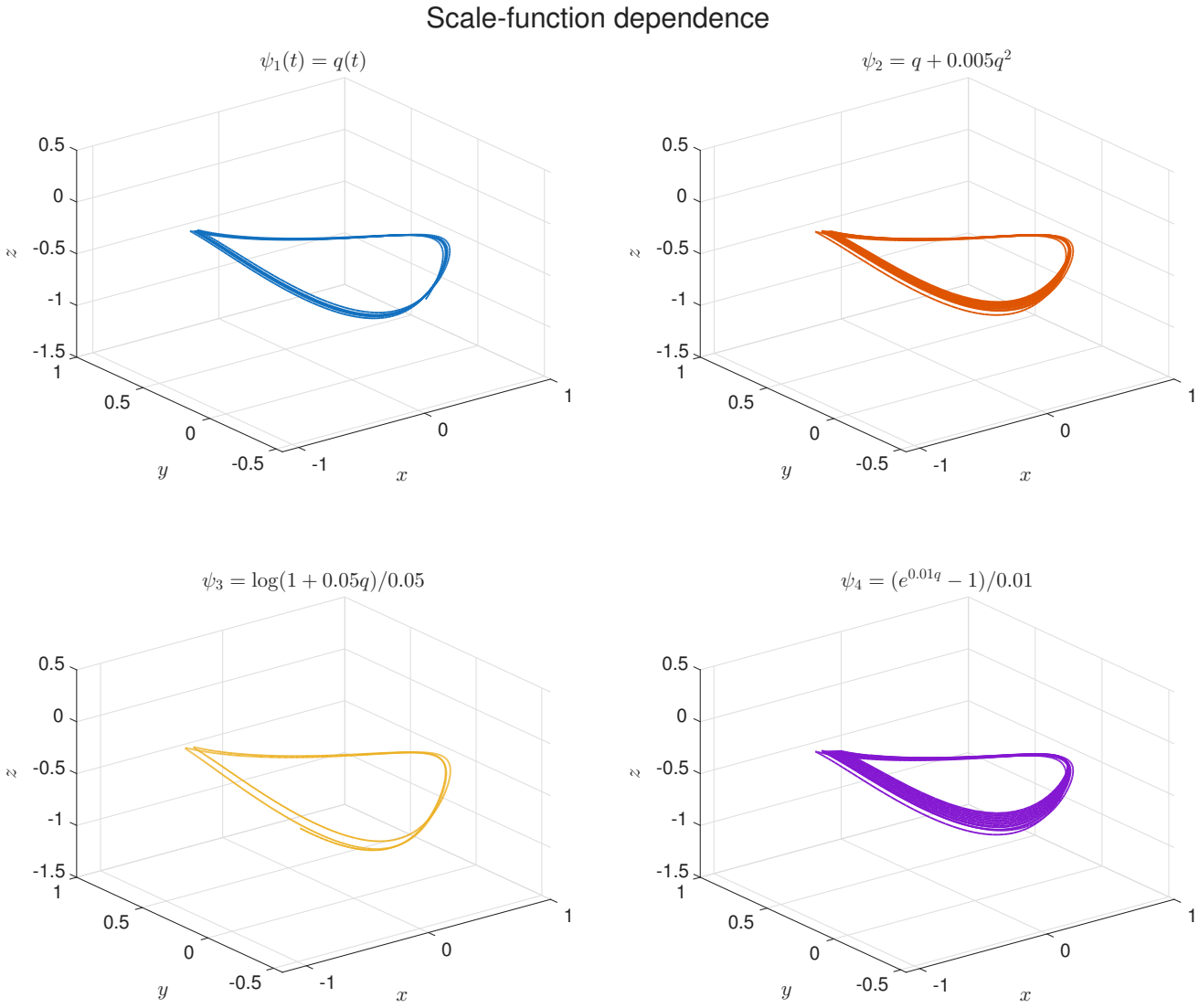

Figure 9. Three-dimensional trajectories for $T = 100$, $N = 1800$, $\gamma = 0.95$, $\theta = 1$, and the four scale functions ψ_1–ψ_4 defined in the text.

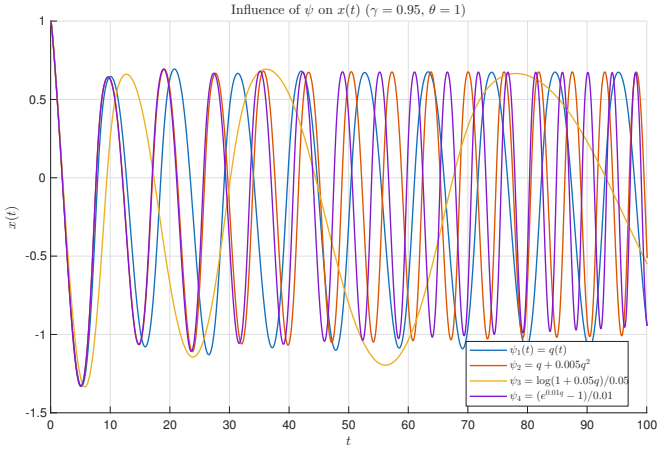

Figure 10. $x(t)$ for $T = 100$, $N = 1800$, $\gamma = 0.95$, $\theta = 1$, under the four operational-time profiles.

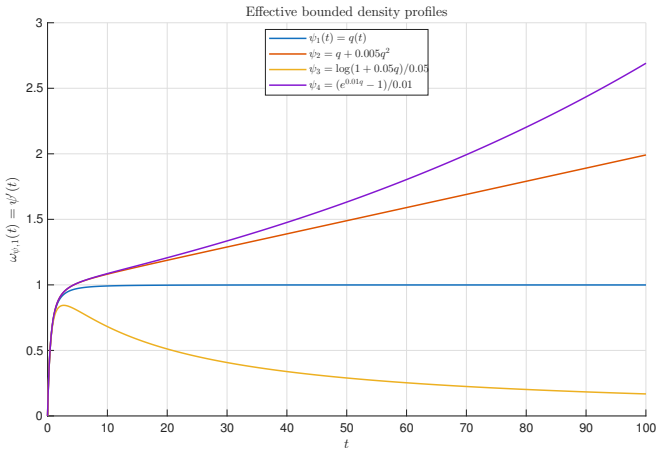

Figure 11. Endpoint-compatible bounded densities $\omega_{\psi,1}(t) = \psi'(t)$ for the four scale functions used in Figures 9 and 10.

Table 4. Post-transient oscillation statistics for the scale-function study ($t \in [10, 100]$, $N = 1800$, $\gamma = 0.95$, $\theta = 1$).

Case	$\psi(T) - \psi(0)$	A_x	A_y	A_z	P_x
Base q	99.010	0.91154	0.63106	0.84382	10.6111
Polynomial in q	148.025	0.90160	0.62028	0.82402	6.3889
Logarithmic in q	35.669	0.94445	0.66826	0.91883	32.6389
Exponential in q	169.150	0.90051	0.61910	0.82153	5.3611

The operational-time span has a pronounced influence on the temporal scale of the oscillation. Relative to the base clock, the polynomial and exponential transformations enlarge $\psi(T) - \psi(0)$ and shorten the median period to 6.3889 and 5.3611, respectively, whereas the logarithmic transformation

compresses the operational span and increases the median period to 32.6389. The corresponding amplitude variations are substantially smaller than these period changes, indicating that the principal sensitivity to ψ in these runs is a time-rescaling effect rather than a large change in attractor size.

In the case of the logarithmic clock, there are just three post-transient peaks in the interval [10, 100]. Thus, its median period is calculated on the basis of two peak distances and should therefore be interpreted as a coarse period estimate rather than a highly averaged statistic.

8.6. Exact convergence benchmark and circuit refinement

A convergence claim should be tested where an exact solution is available. Consider the scalar Volterra problem

$$u(t) = 1 + a_\gamma t + b_\gamma \int_0^t (t-s)^{\gamma-1} s\, ds, \qquad 0 \le t \le 1, \tag{81}$$

which corresponds to the source $g(t) = t$. Its exact solution is

$$u(t) = 1 + a_\gamma t + \frac{b_\gamma}{\gamma(\gamma+1)} t^{\gamma+1}. \tag{82}$$

With

$$\gamma = 0.95, \quad \theta = 1,$$

and the identity clock, the benchmark has $g(0) = 0$ and therefore satisfies the same Volterra endpoint compatibility even though $\psi'(0) = 1$. The numerical errors in Table 5 approach first order, in agreement with Theorem 5.

Table 5. Exact-error convergence test for (81) ($\gamma = 0.95$).

N	error	rate
50	1.278887e-03	–
100	5.793758e-04	1.1423
200	2.741414e-04	1.0796
400	1.330471e-04	1.0430
800	6.548213e-05	1.0228

Figure 12 displays the maximum nodal errors from Table 5 together with the first-order reference slope, providing a visual confirmation of the rate predicted by Theorem 5.

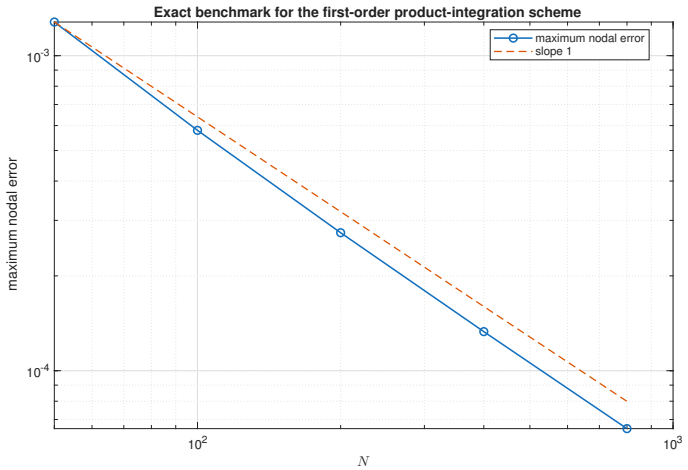

Figure 12. Maximum nodal error for the exact scalar benchmark (81) and (82), with $T = 1$, $\gamma = 0.95$, $\theta = 1$, $\psi(t) = t$, and $N = 50, 100, 200, 400, 800$. The dashed reference has slope one.

However, for the case of the nonlinear circuit, which does not have an exact solution trajectory, and where phase shifts after a long time invalidate pointwise differences, Table 6 keeps track of physically meaningful oscillation statistics. The stabilization of these statistics under refinement supports the computed long-time behavior without calling nonmonotone pointwise differences a convergence order. In particular, from $N = 1800$ to $N = 3600$, the relative changes in A_x, A_y, and A_z are approximately 0.004%, 0.14%, and 0.08%, respectively, while the median period changes by about 0.26%.

Table 6. Application-level refinement for the circuit with $T = 100$, $\gamma = 0.95$, $\theta = 1$, and $\psi(t) = t^2/(1 + t)$; statistics use $t \in [10, 100]$.

N	h	A_x	A_y	A_z	P_x
450	0.22222	0.91168	0.64112	0.85777	10.4444
900	0.11111	0.91161	0.63352	0.84625	10.6667
1800	0.05556	0.91154	0.63106	0.84382	10.6111
3600	0.02778	0.91151	0.63019	0.84316	10.6389

The three model elements cannot be considered equivalent: γ will modify the memory function and the AB coefficients, θ will modify the fractal exponent, and ψ will modify the operational-time trajectory. A future identification of the physical nature of this model must therefore calibrate the impact of these elements against real circuit data, rather than assume some arbitrary value of ψ.

9. Conclusions

This study formulates a nonlinear integrator circuit governed by the ABFF outer derivative. The nomenclature is distinct from the well-known operators ABC and ABR, and the singular expressions are considered only within the range of $0 < \gamma < 1$, where $\gamma = 1$ is the limit value. The $U - U_0$

regularization transforms the original ABR-type system into the weighted ABC/Volterra integral equation.

Two improvements have been made to the analysis. The first is that uniqueness, continuous dependence, and Ulam–Hyers stability are based on the contraction constant $\eta = a_\gamma M_\omega L_F < 1$ combined with fractional Gronwall estimates, instead of a bound increasing in T^γ. Continuation criteria are clear about the required boundedness for existence. The second is that generalized Ulam–Hyers–Rassias stability holds in a weighted norm with a new constant q_φ. On the numerical side, a discrete weakly singular stability lemma and a global $O(h)$ convergence theorem complement the consistency calculation, and an exact benchmark exhibits rates tending to one.

The reported simulations were also redesigned to match both the bounded-density hypothesis and the necessary endpoint compatibility $\omega_{\psi,\theta}(0)F(U_0) = 0$. Because the prescribed initial circuit state is not an equilibrium, every fractional circuit run now uses a clock with zero endpoint density. The base choice is $\psi_b(t) = t^2/(1 + t)$, and the scale-function study uses monotone transformations of this base clock that preserve $\psi_i'(0) = 0$. Terminal coordinates and the parameter-independent maximum norm are replaced by post-transient amplitudes and periods. Finally, ψ is interpreted as a phenomenological operational-time map. The present paper does not claim a new fabricated circuit or SPICE realization of arbitrary analytic clocks; experimental calibration and controlled hardware realization are natural directions for future work.

Author contributions

All authors contributed equally to formal analysis, software, conceptualization, methodology, writing–original draft, and writing–review and editing. All authors have read and approved the final version of the manuscript for publication.

Use of Generative-AI tools declaration

The authors declare they have not used Artificial Intelligence (AI) tools in the creation of this article.

Acknowledgments

The researchers would like to thank the Deanship of Graduate Studies and Scientific Research at Qassim University (https://www.qu.edu.sa) for financial support (QU-APC-2026).

Conflict of interest

The authors declare no conflicts of interest.

References

1. I. Podlubny, *Fractional differential equations*, Academic Press, 1999.
2. A. A. Kilbas, H. M. Srivastava, J. J. Trujillo, *Theory and applications of fractional differential equations*, Elsevier, 2006.

3. K. Diethelm, *The analysis of fractional differential equations*, Springer, 2010. https://doi.org/10.1007/978-3-642-14574-2
4. F. Mainardi, *Fractional calculus and waves in linear viscoelasticity*, Imperial College Press, 2010. https://doi.org/10.1142/P614
5. I. Petráš, *Fractional-order nonlinear systems: modeling, analysis and simulation*, Springer, 2011. https://doi.org/10.1007/978-3-642-18101-6
6. M. Caputo, M. Fabrizio, A new definition of fractional derivative without singular kernel, *Progress Fractional Differ. Appl.*, **1** (2015), 73–85. https://doi.org/10.12785/pfda/010201
7. J. Losada, J. J. Nieto, Properties of a new fractional derivative without singular kernel, *Progress Fractional Differ. Appl.*, **1** (2015), 87–92. https://doi.org/10.12785/pfda/010202
8. J. Singh, D. Kumar, Z. Hammouch, A. Atangana, A fractional epidemiological model for computer viruses pertaining to a new fractional derivative, *Appl. Math. Comput.*, **316** (2018), 504–515. https://doi.org/10.1016/j.amc.2017.08.048
9. M. Alqhtani, L. Sadek, K. M. Saad, The Mittag-Leffler–Caputo–Fabrizio fractional derivative and its numerical approach, *Symmetry*, **17** (2025), 800. https://doi.org/10.3390/sym17050800
10. L. Sadek, I. Aldawish, An efficient numerical approach for solving the Mittag–Leffler fractional differential equations, *Math. Sci.*, **20** (2026), 3. https://doi.org/10.57647/mathsci.2026.2003.14
11. A. Atangana, D. Baleanu, New fractional derivatives with nonlocal and non-singular kernel: theory and application to heat transfer model, *Ther. Sci.*, **20** (2016), 763–769. https://doi.org/10.2298/TSCI160111018A
12. F. Jarad, T. Abdeljawad, Z. Hammouch, On a class of ordinary differential equations in the frame of Atangana–Baleanu fractional derivative, *Chaos Solitons Fract.*, **117** (2018), 16–20. https://doi.org/10.1016/j.chaos.2018.10.006
13. A. Atangana, Fractal-fractional differentiation and integration: connecting fractal calculus and fractional calculus to predict complex systems, *Chaos Solitons Fract.*, **102** (2017), 396–406. https://doi.org/10.1016/j.chaos.2017.04.027
14. A. Akgül, S. Ahmad, A. Ullah, D. Baleanu, E. K. Akgül, A novel method for analysing the fractal fractional integrator circuit, *Alex. Eng. J.*, **60** (2021), 3721–3729. https://doi.org/10.1016/j.aej.2021.01.061
15. K. Zourmba, C. Fischer, B. Gambo, J. Y. Effa, A. Mohamadou, Fractional integrator circuit unit using Charef approximation method, *Int. J. Dyn. Control*, **8** (2020), 943–951. https://doi.org/10.1007/s40435-020-00621-2
16. B. T. Krishna, Studies on fractional order differentiators and integrators: a survey, *Signal Process.*, **91** (2011), 386–426. https://doi.org/10.1016/j.sigpro.2010.06.022
17. I. Podlubny, I. Petráš, B. M. Vinagre, P. O'Leary, L. Dorčák, Analogue realizations of fractional-order controllers, *Nonlinear Dyn.*, **29** (2002), 281–296. https://doi.org/10.1023/A:1016556604320
18. L. Chua, Memristor—the missing circuit element, *IEEE Trans. Circuit Theory*, **18** (1971), 507–519. https://doi.org/10.1109/TCT.1971.1083337

19. D. B. Strukov, G. S. Snider, D. R. Stewart, R. S. Williams, The missing memristor found, *Nature*, **453** (2008), 80–83. https://doi.org/10.1038/nature06932
20. L. Chua, Resistance switching memories are memristors, *Appl. Phys. A*, **102** (2011), 765–783. https://doi.org/10.1007/s00339-011-6264-9
21. J. J. Yang, D. B. Strukov, D. R. Stewart, Memristive devices for computing, *Nature Nanotechnol.*, **8** (2013), 13–24. https://doi.org/10.1038/nnano.2012.240
22. L. Sadek, A. S. Bataineh, E. M. Sadek, I. Hashim, A general definition of the fractal derivative: theory and applications, *AIMS Math.*, **10** (2025), 15390–15409. https://doi.org/10.3934/math.2025690
23. R. Almeida, A Caputo fractional derivative of a function with respect to another function, *Commun. Nonlinear Sci. Numer. Simul.*, **44** (2017), 460–481. https://doi.org/10.1016/j.cnsns.2016.09.006
24. J. V. da C. Sousa, E. C. de Oliveira, On the ψ-Hilfer fractional derivative, *Commun. Nonlinear Sci. Numer. Simul.*, **60** (2018), 72–91. https://doi.org/10.1016/j.cnsns.2018.01.005
25. B. S. T. Alkahtani, Chua's circuit model with Atangana–Baleanu derivative with fractional order, *Chaos Solitons Fract.*, **89** (2016), 547–551. https://doi.org/10.1016/j.chaos.2016.03.020
26. A. Atangana, I. Koca, Chaos in a simple nonlinear system with Atangana–Baleanu derivatives with fractional order, *Chaos Solitons Fract.*, **89** (2016), 447–454. https://doi.org/10.1016/j.chaos.2016.02.012
27. R. Garrappa, Numerical solution of fractional differential equations: a survey and a software tutorial, *Mathematics*, **6** (2018), 16. https://doi.org/10.3390/math6020016
28. J. D. Djida, I. Area, A. Atangana, Numerical computation of a fractional derivative with non-local and non-singular kernel, *Math. Model. Nat. Phenom.*, **12** (2017), 4–13. https://doi.org/10.1051/mmnp/201712302
29. M. Toufik, A. Atangana, New numerical approximation of fractional derivative with non-local and non-singular kernel: application to chaotic models, *Eur. Phys. J. Plus*, **132** (2017), 444. https://doi.org/10.1140/epjp/i2017-11717-0
30. A. Akgül, A novel method for a fractional derivative with non-local and non-singular kernel, *Chaos Solitons Fract.*, **114** (2018), 478–482. https://doi.org/10.1016/j.chaos.2018.07.032

AIMS Press